Cold Regions Science and Technology 125 (2016) 1–11

Contents lists available at ScienceDirect

Cold Regions Science and Technology

journal homepage: www.elsevier.com/locate/coldregions

Speed and attenuation of acoustic waves in snow: Laboratory experiments and modeling with Biot's theory

Achille Capelli [a,*], Jagdish C. Kapil [a,b], Ingrid Reiweger [a], Dani Or [c], Jürg Schweizer [a]

[a] *WSL Institute for Snow and Avalanche Research SLF, Flüelastrasse 11, CH-7260 Davos Dorf, Switzerland*
[b] *Snow and Avalanche Study Establishment (SASE), Chandigarh (UT) 160036, India*
[c] *Department of Environmental Sciences, ETH Zurich, Universitätsstrasse 16, CH-8092, Zurich, Switzerland*

ARTICLE INFO

Article history:
Received 6 August 2015
Received in revised form 4 December 2015
Accepted 22 January 2016
Available online 29 January 2016

Keywords:
Mechanical properties of snow
Snow acoustics
Acoustic emissions
Elastic modulus
Sound propagation

ABSTRACT

Monitoring acoustic emissions (AE) prior to imminent failure is considered a promising technique for assessing snow slope instability. Gaps in elastic wave propagation characteristics in snow hinder quantitative interpretation of AE signals. Our study focuses on characterizing the propagation of acoustic reference signals in the ultrasonic range across cylindrical snow samples with varying density (240–450 kg m^{-3}). We deduced the acoustic attenuation coefficient within snow by performing experiments with different column lengths to eliminate possible influences of the snow-sensor coupling. The attenuation coefficient was measured for the entire burst signal and for single frequency components in the range of 8 to 35 kHz. The acoustic wave propagation speed, calculated from the travel time of the acoustic signal, varied between 300 m s^{-1} and 950 m s^{-1}, depending on the density and hardness of snow. From the sound speed we also estimated the Young's modulus of our snow samples; the values of the modulus ranged from 30 to 340 MPa for densities between 240 and 450 kg m^{-3}. In addition, we modeled the sound propagation for our experimental setup using Biot's model for wave propagation in a porous medium. The model results were in good agreement with our experimental results and suggest that our acoustic signals consisted of Biot's slow and fast waves. Our results can be used to improve the identification and localization of acoustic emission sources within snow in view of assessing snow slope instability.

1. Introduction

Snow avalanches present a significant hazard for human activity and infrastructure in snow-covered mountainous regions world-wide, yet, to date, the precise time and location of a single avalanche event remain unpredictable (e.g., McClung and Schaerer, 2006; Schweizer, 2008). For the prediction of instability of a snow-covered slope, suitable precursors must be identified. Among the most promising precursors are acoustic emissions (AE) generated during the formation of micro-cracks or the breaking of ice bonds within the snow (Reiweger et al., 2015; Reiweger and Schweizer, 2013). Current research efforts focus on the identification and localization of acoustic emission features preceding snow failure and avalanches. The knowledge of the speed and the attenuation of acoustic waves in snow is, however, a necessary prerequisite to increase the accuracy of event localization and to describe the mechanism of evolution of the acoustic signals from the emission to the detection.

Oura (1953) was among the first to measure the speed of sound in snow. Since then various studies were performed, but the results on the acoustic properties of snow widely vary depending on the measurement method. When piezoelectric sensors in direct contact to the snow were used, the obtained speed was higher than the sound speed in air and increased with increasing density (solid symbols in Fig. 1, Reiweger et al., 2015; Smith, 1965; Takei and Maeno, 2004; Yamada et al., 1974). When, on the other hand, the speed was measured with an impedance tube (Buser, 1986; Ishida, 1965; Marco et al., 1998) or with microphones not in direct contact with the snow's ice skeleton (Gudra and Najwer, 2011; Iwase et al., 2001; Lee and Rogers, 1985; Oura, 1953), the measured speed was lower than the speed in air and decreased with increasing density (open symbols, Fig. 1).

In Fig. 1, the values of the speed of sound previously determined in various studies are compiled as a function of snow density. As already shown by Sommerfeld (1982), three distinct speed patterns can be observed for densities higher than about 250 kg m^{-3}. Sommerfeld and Gubler (1983) connected them to longitudinal and transversal waves propagating in the ice skeleton (solid symbols, Fig. 1) and longitudinal waves propagating in the air phase (open symbols). Ishida (1965) showed that the speed in the air phase depends on the frequency in the range of 0.1 to 10 kHz and is proportional to the air permeability of snow. With increasing density the pore space becomes more tortuous and the air permeability decreases; accordingly the speed of the acoustic wave propagating in the air phase decreased (Ishida, 1965). Lee and Rogers (1985) suggested that a transition in the propagation phase

---

* Corresponding author. Tel.: +41 81 417 0252; fax: +41 81 417 0110.
E-mail address: achille.capellli@slf.ch (A. Capelli).

http://dx.doi.org/10.1016/j.coldregions.2016.01.004
0165-232X/

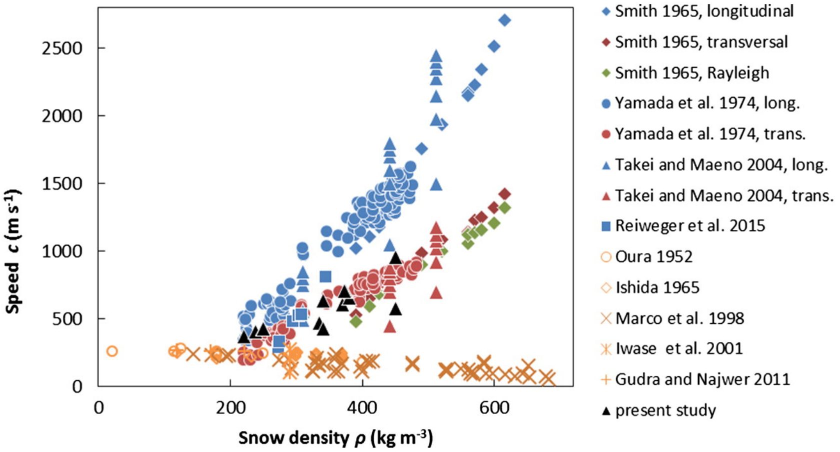

Fig. 1. Summary of sound propagation speed values from previous studies. The solid symbols represent values obtained with sensors in direct contact with the snow. The open symbols represent values obtained with microphones not in direct contact with the snow. Three different wave types were observed: longitudinal (blue) and transversal (red) waves propagating in the ice skeleton, and waves propagating in the pore space (orange). The green diamonds represent the measured velocities of Rayleigh waves (Smith, 1965). In addition, the results of our own measurements are shown (black triangles). (For interpretation of the references to color in this figure legend, the reader is referred to the web version of this article.)

exists at a density of about 300 kg m^{-3}, with waves propagating mainly in the air phase for lower density and mainly in the ice skeleton for higher density snow. However, Marco et al. (1998) measured the speed of waves in the air phase at densities up to 680 kg m^{-3} contradicting the assumption of Lee and Rogers (1985). Takei and Maeno (2004) showed that the wave speed in the ice skeleton is determined by the elastic moduli of the snow, which are determined by the microstructure. The velocities of the longitudinal and transversal waves in the ice skeleton increased during temperature cycles due to the increased strength of the bonds between the ice grains. When the temperature approached 0 °C, the weakening of the bonds caused a drop in the wave speed. Yamada et al. (1974) found that the sound speed is anisotropic for anisotropic snow.

The attenuation of acoustic waves in snow was a topic of various studies in the past. The attenuation properties were usually either obtained from the transmission loss at different snow thicknesses (Gudra and Najwer, 2011; Ishida, 1965; Reiweger et al., 2015) or deduced from the measured impedance (Marco et al., 1998). Lang (1976), Johnson (1982), and Kapil et al. (2014) measured the attenuation of acoustic waves in snow without explicitly reporting the attenuation coefficient, but it can still be derived from their published data. The attenuation coefficient measured by the different authors was between 0.05 and 3.5 dB cm^{-1}. A direct comparison of the published values is difficult, since different methods were applied on different snow types in different frequency ranges. The attenuation was found to increase with increasing frequency (Ishida, 1965; Iwase et al., 2001) and also with increasing snow density (Gudra and Najwer, 2011; Ishida, 1965; Marco et al., 1998). Ishida (1965) suggested that the attenuation was inversely proportional to the square root of the air permeability.

Most previous models for sound propagation in snow assume a rigid ice frame (e.g. Buser, 1986). Buser (1986) reproduced the measured surface impedance with the model of Zwikker and Kosten (1949). The same model was used to investigate the relationship between acoustic properties and snow microstructure by Attenborough and Buser (1988) and Marco et al. (1998). Boeckx et al. (2004) applied the Johnson-Champoux-Allard model (Allard and Attala, 2009; Champoux and Allard, 1991; Johnson et al., 1987) to the propagation of sound above snow covered terrain. Maysenhölder et al. (2012) studied the relation between microstructure and sound absorption with the relaxation model of Wilson (1993, 1997). These models were successfully applied to experiments where the air–snow interaction was studied, although the ice frame is considered to be rigid. On the other hand, Biot's model (Biot, 1956a) takes into account the combined motion of the elastic ice frame and the pore fluid/gas and was applied to snow by Johnson (1982). It provides two types of longitudinal waves (fast and slow Biot's waves) and one type of transversal wave as it is experimentally observed. The experimental data available to Johnson (1982) tended to support the model predictions, but further experiments were required to properly evaluate Biot's model on snow. More recently, Sidler (2015) modeled the propagation of acoustic waves in snow with Biot's theory. He simplified the approach by expressing the many parameters required as a function of snow porosity only and found that for low-density snow (below 200 kg m^{-3}) the speed of the Biot's slow waves exceeds the speed of Biot's fast waves. This is in agreement with the experimental data presented in Fig. 1. Also the propagation of waves produced during blasting experiments was modeled above and inside the snowpack with Biot's model for the frequency range of 0 to 1 kHz (Sidler et al., 2016; Simioni et al., 2015). Sidler et al. (2016) successfully reproduced the acceleration measured in the snowpack and showed that the waves propagating through the pore space, i.e. slow Biot's waves, significantly contribute to wave propagation in snow due to an explosion.

The acoustic propagation properties can be used to derive different mechanical snow properties, e.g. the elastic moduli can be derived from the propagation speed (Smith, 1965; Takei and Maeno, 2004). The most basic method to measure Young's modulus is a direct mechanical test either quasi-static (Mellor, 1975) or dynamic (Sigrist, 2006). Alternatively, the elastic properties can be derived from micro-computed tomography images (Schneebeli, 2004), or derived from the snow micro-penetrometer (SMP) penetration force signal (Marshall and Johnson, 2009). The values obtained with the different methods differ substantially, e.g. the values obtained with the micro-computed tomography are about three orders of magnitude larger than the values derived from SMP signal (Reuter et al., 2013). The difference is attributed to the different strain rates and magnitudes of displacement applied during the different measurements. With some of the methods non-elastic deformation will be induced, typically resulting in lower values of the modulus. Alternatively, acoustic waves cause small strains at high rates in the elastic range. Therefore, the acoustic method for the derivation of the Young's modulus seems a feasible option, even superior to other methods. In particular, the AE method allows a non-destructive and in-situ characterization of the mechanical properties of snow.

The values of speed and attenuation of acoustic waves published in previous studies vary strongly with the snow properties and considerably depend on the measurement method employed. Most of the previous results were obtained at frequencies below 10 kHz, while recent snow failure experiments indicate that the relevant AE are in the ultrasound range with peak frequencies between 20 and 500 kHz (Datt et al., 2015; Reiweger et al., 2015; Scapozza et al., 2004). For the identification and localization of AE features preceding snow failure a good understanding of the propagation of acoustic waves in snow is needed and a model applicable for a wide range of snow types must be found.

Our objectives are to (1) measure the propagation speed and the attenuation coefficient of acoustic waves in snow for frequencies above 10 kHz, (2) model the wave propagation, and (3) relate the propagation characteristics of acoustic waves to the Young's modulus. Therefore, we measured the speed and the attenuation of short broad-band pulses generated by a pencil lead fracture (PLF) traveling through small snow columns in the laboratory, and modeled the wave propagation for our experimental setup using Biot's model. Furthermore, we derived the Young's modulus from the speed of the acoustic waves traveling in the ice skeleton and studied its change due to changes of the microstructure with time.

2. Methods

We measured the speed and attenuation of acoustic waves propagating through a snow column in a cold laboratory following the method described by Reiweger et al. (2015). Our signals were short broad-band pulses generated by a pencil lead fracture (PLF). The signal attenuation was derived from the magnitude of the signal at different column length, canceling out the effects of the sensor coupling. The results were compared to the values obtained from Biot's model.

2.1. Experimental setup

The experimental setup is illustrated in Fig. 2. A snow column (diameter: 14.5 cm, length: 20 to 40 cm) was placed between two aluminum plates. On each of the plates an acoustic sensor was attached with silicon glue; sensor S1 on the top and sensor S2 below the snow column. The dimensions of the top plate were 126 mm × 126 mm × 6 mm, and of the bottom plate 278 mm × 180 mm × 6 mm. A third sensor S3 was glued to a brass ring (460 mm × 20 mm × 0.8 mm) fixed around the snow column 25 mm above the bottom plate. The plates and the brass ring were used as waveguides to increase the coupling of the sensors to the snow (Kapil et al., 2014; Reiweger et al., 2015). The acoustic sensors have a preferential sensitivity to out of plane waves. Therefore, the sensor S2 on the bottom plate should detect longitudinal waves, while the sensor S3 on the ring at the side of the column should detect transversal waves. At all positions wideband piezoelectric acoustic sensors (Mistras WD, 20–1000 kHz) were used. The sampling rate was 2000 kHz.

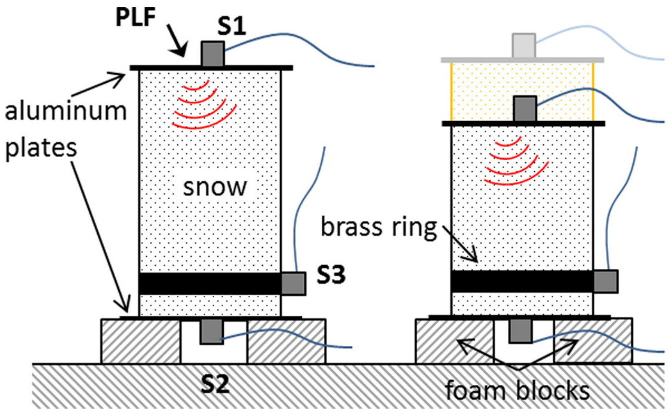

Fig. 2. Experimental setup for the measurement of the propagation speed and attenuation across snow columns. The speed was determined from the travel time. The attenuation was derived from the magnitude of the signal at different column lengths (8 to 40 cm).

To improve the acoustic coupling between the snow and the metal plates, a thin layer of ice or grease was used. The ice layer was created by putting the snow in contact with the warmer metal plates. A part of the snow melted and subsequently refroze, creating an ice layer that stuck to the plate. Using the ice layer was more time consuming than using grease, but the obtained coupling quality was more reproducible. Grease was used as couplant between the metal ring and the snow. The whole setup was placed on two plastic foam blocks to attenuate possible external noise.

The acoustic pulse was produced by breaking a pencil lead tip (diameter 0.5 mm, length 3 mm, HB, ASTM E976) on the top plate (PLF or Hsu-Nielsen source) at approximately 10 mm from the sensor S1. The PLF creates a short broad-band acoustic pulse (Grosse and Ohtsu, 2006; Higo and Inaba, 1991).

The acoustic signals were recorded with an AE recording system from Physical Acoustics. A more detailed description of the recording system can be found in Reiweger et al. (2015). The working principle is the following: Every time the measured voltage signal exceeds a fixed threshold (e.g. when a PLF pulse reaches a sensor) the recording system is activated, a waveform is recorded and several AE features, such as signal amplitude and energy, are extracted. The amplitude is defined as the maximum amplitude of the registered waveform. The energy is the integral of the squared voltage signal over the signal duration (Fig. 3a) divided by a reference resistance (10 kOhm). The duration of the registered signal depends on how long the measured signal stays above the threshold. For a more detailed description and the definition of the AE parameters the reader is referred to Grosse and Ohtsu (2006).

2.2. Measurement of speed and attenuation coefficient

The speed of the longitudinal waves was obtained by dividing the column length h by the travel time t, which is the difference between the arrival time at sensor S1 (mounted at the top) and the sensor S2 (mounted at the bottom):

$$c_{\text{snow}} = \frac{h}{t} \tag{1}$$

For the speed of the transversal waves the distance between the sensor S1 and the sensor S3 (mounted on the lateral surface) was divided by the difference of the arrival times. The speed of at least 10 PLF signals (Table 1) was measured and averaged. The arrival time was determined as the first crossing of a fixed threshold (Fig. 3a). The arrival time determined with a fixed threshold depends on the signal magnitude, i.e. if the signal is stronger attenuated, the amplitude is lower and with the threshold method a later arrival time is measured. To avoid this problem, the Akaike information criterion (AIC) as proposed by Kurz et al. (2005) was applied to improve the precision of arrival time determination.

The wave energy U decays exponentially over the column length h:

$$U(h) \sim e^{-\alpha_{en}\, h} \tag{2}$$

To measure the attenuation coefficient α_{en}, the experiment was repeated with different column lengths (40 to 8 cm, see Fig. 2). Comparing the signals obtained for the different column lengths, the evolution of the signal in the missing snow portion can be determined independently of the effects of the sensor coupling. This method is valid under the assumption that the signal distortion at the snow-sensor transition is linear and that the sensor-snow coupling is unvaried. In this way it was possible to eliminate the distortions of the signal occurring at the transition between snow, metal plate, and sensor. The attenuation coefficient α_{en} of the entire pulse was obtained from a linear fit of the entire signal energy in dB over the column length (Fig. 3b). The mean value of at least 10 PLF signals, and at least 6 column lengths were used for the fit (Table 1). The slope of the linear fit in the semi-logarithmic plot is the

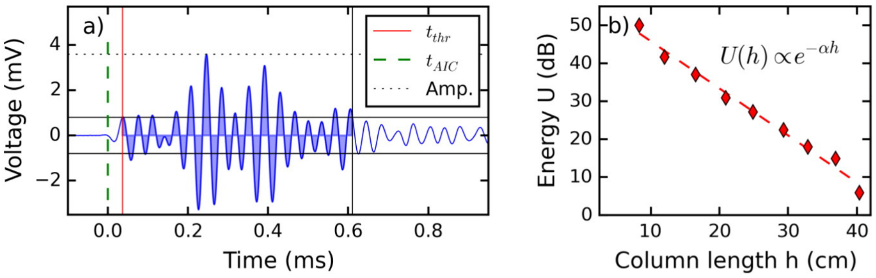

Fig. 3. (a) Example of arrival time picking and AE features extraction. The arrival time is first determined by the first threshold crossing (t_{thr}). Then the precision is improved with the AIC method (t_{AIC}). The amplitude is defined as the maximum signal amplitude. The energy is equal the blue surface in the plot. (b) Example of exponential decrease of the energy over the column length and linear fit to obtain the attenuation coefficient (semi-logarithmic plot).

attenuation coefficient (given in dB cm^{-1}). In addition, the attenuation coefficient was obtained also from the signal amplitude (α_{amp}). In this case the slope of the fitted line was multiplied by 2 since the energy is proportional to the square of the amplitude.

The attenuation coefficient depends on the frequency. Therefore, the attenuation at the single frequencies $\alpha(\omega)$ was obtained from the power spectra at the different column lengths. The power spectrum indicates the distribution of the energy over the single frequency component. The average power spectrum of several signals was computed at each distance. Furthermore, the obtained mean power spectrum was smoothened with the weighted moving average with window size 10 kHz and Gaussian form. The frequency dependent attenuation coefficient $\alpha(\omega)$ was obtained from a fit of the averaged and smoothened power spectrum over the different distances for each discrete frequency ω.

2.3. Sample preparation

The homogeneous snow columns (Samples Col1 to Col42) were prepared from nature identical snow produced by SLF's snow making machine (Schleef et al., 2014). The snow was sieved into a plastic tube with 145 mm diameter. Samples with different densities were obtained by varying compression of the snow in the tube. Samples with different grain sizes were prepared using sieves with different mesh sizes (1 mm, 1.4 mm, and 2.2 mm). The inner surface of the tube was sprayed with a lubricant oil to avoid freezing of the snow to the tube. The samples were removed from the tube after at least one day during which the ice grains sintered. The samples were 20 to 40 cm long and the diameter was 14.5 cm. The snow characteristics of the single samples are presented in Table 1.

2.4. Influence of sintering and temperature

To investigate the influence of snow sintering and temperature on the propagation speed we performed two kinds of experiments. In a first experiment (Col41 and Col42), two snow columns with different density and grain size were prepared sieving the snow first through a sieve with a mesh size of 2.2 mm and then through one with 1 mm mesh size. The snow with grains smaller than 1 mm was used for the sample Col41 and the snow with grain size between 1 mm and 2.2 mm was used for sample Col42. After one day of sintering the samples were extracted from the tube and mounted in the measurement setup. The temperature of the cold laboratory was increased stepwise during three days from −21 °C to −5 °C. Subsequently, the temperature was kept at −5 °C during four days and then decreased during another three days stepwise to −20 °C. The sound speed was measured at each temperature without changing the setup so that observed changes should be only due to changes of the snow properties. The column length was 15.7 cm for sample Col41 and 16.5 cm for Col42. The attenuation coefficient was not determined for these experiments since this

Table 1

Summary of the snow properties and the experimental results for the different snow samples. The snow properties are: temperature T, density ρ, grain shape F, grain size D, hand hardness index R, and sintering time t_s. The maximum column length h, the number of measured lengths, and the number of PLF for each length are listed. The speed c was measured with the sensor S2 with a column length of about 150 mm. The attenuation coefficients of the entire pulse energy α_{en} and of the maximum amplitude α_{amp} are shown with the corresponding coefficients of determination R^2 (except for samples Col41 and Col42). The minimum and the maximum of the frequency dependent attenuation $\alpha(\omega)$ in the frequency range of 10 to 35 kHz are listed. The fitting parameters of Biot's model are the permeability κ, the pore characteristic size d, and the structure factor $\overline{d}$. The Young's modulus E was derived from the wave speed, with a fixed value of the Poisson's ratio $\nu = 0.25$ (Mellor, 1975).

Sample		Col1	Col2	Col3A	Col3B	Col3C	Col41	Col42	Sam11	Sam12	Sam13	Sam14
$\boldsymbol{T}$	(°C)	−20	−20	−9.5	−5.5	−15.5	−(20–5)	−(20–5)	−8.5	−8.5	−8.5	−8.5
$\boldsymbol{\rho}$	kg m^{-3}	334	221	238	250	249	450	340	369	380	374	372
$\boldsymbol{F}$	–	DF	DF	–	–	–	RG	RG	RG	RG	RG	RG
$\boldsymbol{D}$	mm	0.75–1	1	1	1	1	0.25–0.75	1–2	0.5–1	0.5–1	0.5–1	0.5–1
$\boldsymbol{R}$	–	1–2	–	–	–	–	4–5	3–4	–	–	–	–
$\boldsymbol{t_s}$	h	48	552	144	192	144	22–240	22–240	20	44	68	92
max. $\boldsymbol{h}$	cm	40	35	30	30	30	16	16.5	20.5	21	19.5	19.5
# lengths	–	9	9	6	5	7	1	1	12	10	10	10
# PLF	–	20	30	20	20	20	20	20	10	10	10	10
$\boldsymbol{c}$	m s^{-1}	470 ± 4	370 ± 12	407 ± 8	434 ± 12	431 ± 28	580–950	425–635	604 ± 18	658 ± 10	705 ± 15	709 ± 27
$\boldsymbol{\alpha_{en}}$	dB cm^{-1}	1.2 ± 0.1	0.79 ± 0.03	0.6 ± 0.1	0.98 ± 0.05	0.7 ± 0.1	–	–	0.60 ± 0.13	0.81 ± 0.12	1.15 ± 0.30	0.35 ± 0.12
$\boldsymbol{R^2_{en}}$	–	0.987	0.995	0.892	0.991	0.898	–	–	0.683	0.858	0.644	0.532
$\boldsymbol{\alpha_{amp}}$	dB cm^{-1}	1.1 ± 0.1	0.77 ± 0.1	0.6 ± 0.1	1.01 ± 0.04	0.8 ± 0.1	–	–	0.57 ± 0.16	0.74 ± 0.12	0.79 ± 0.22	0.25 ± 0.22
$\boldsymbol{R^2_{amp}}$	–	0.95	0.921	0.886	0.984	0.924	–	–	0.553	0.826	0.608	0.143
$\mathbf{min}(\boldsymbol{\alpha}(\boldsymbol{\omega}))$	dB cm^{-1}	0.67	0.4	0.41	0.91	0.30	–	–	–	–	–	–
$\mathbf{max}(\boldsymbol{\alpha}(\boldsymbol{\omega}))$	dB cm^{-1}	1.53	1.3	1.23	1.34	1.61	–	–	–	–	–	–
$\boldsymbol{\kappa}$	s m^2 kg^{-1}	3.1×10^{-4}	5×10^{-4}	3.6×10^{-4}	3.25×10^{-4}	4×10^{-4}	–	–	–	–	–	–
$\boldsymbol{d}$	mm	0.3	0.35	0.21	0.25	0.3	–	–	–	–	–	–
$\boldsymbol{\overline{d}}$	–	1	1	1	1	1	–	–	–	–	–	–
$\boldsymbol{E}$	MPa	61 ± 0.5	25.2 ± 0.8	33 ± 0.6	39 ± 1	38.5 ± 2.5	125–340	54–115	114 ± 7	135 ± 4	155 ± 7	157 ± 12

would have required to successively shorten the columns and would have prevented studying the effect of sintering and temperature.

For the second experiment (Sam11 to Sam14) a snow block of 70 cm × 40 cm × 20 cm was prepared by sieving natural snow (mesh size 2.2 mm) in a box. The snow had been collected at the Flüelapass (near Davos, Switzerland) three days before and stored at -25 °C. The sample was then stored for one day at -8 ± 1 °C, and a vertical rectangular column (13 cm × 13 cm × 20 cm) was cut out and the wave speed and the attenuation coefficient were measured. The measurement was repeated on a new column each day during four days. The density of the snow block was 375 ± 15 kg m^{-3} and was found to not change significantly over the four days. In addition, snow micro-penetrometer (SMP) (Schneebeli and Johnson, 1998; Johnson and Schneebeli, 1999) measurements were done in the part of the snow block that was not used for the acoustic measurements at one hour intervals during the first 4 h and then after each acoustic measurement. An effective elastic modulus was then derived from the SMP signal as described by Marshall and Johnson (2009). Moreover, the SMP measurements allowed detecting density variations within the samples. Density profiles were hence derived from the SMP signals following Proksch et al. (2015). The mean density over the 20 profiles was 415 ± 34 kg m^{-3}, i.e. about 10% higher than the manually measured density. No substantial trend in the vertical direction was found. The mean standard deviation of the density in the vertical direction for the single profiles was 6%. Therefore, we consider the samples to be uniform. Furthermore, the SMP measurements indicated that the density did not change over time.

2.5. Biot's model

The model by Biot (1956a) and Biot (1956b) was developed to describe the propagation of waves in a porous medium and considers the interaction of the elastic solid phase (ice) and the viscous fluid/gas phase (air). Biot's model was previously applied to snow by Johnson (1982), using the analytical solution of Deresiewicz and Rice (1962). Assuming planar waves propagating in a homogeneous, isotropic, fluid saturated, poroelastic material, the model predicts the existence of two uncoupled dilatational waves and one transversal wave (Fig. 4). The first kind of longitudinal waves, also called fast waves, and the transversal waves are just slightly dispersive, while the second kind of longitudinal waves or slow waves are dispersive. All Biot's waves are considerably attenuated — increasing with increasing frequency. However, slow waves have much higher attenuation coefficient than the other wave kinds (4 to 7 orders of magnitude higher). The detailed derivation of Biot's model and the application to snow has previously been described (Biot, 1956a; Biot, 1956b; Deresiewicz and Rice, 1962; Johnson, 1982; Sidler, 2015). Deresiewicz and Rice (1962) found an analytical solution for plane waves, which was applied to snow by Johnson (1982).

The equations for the complex frequency dependent wave numbers $k(\omega)$ are given in the Appendix. From Eqs. A1 and A2 the speed ($c(\omega) = \frac{\omega}{\mathrm{Re}(k(\omega))}$) and the attenuation factor ($\alpha(\omega) = \mathrm{Im}(k(\omega))$) can be obtained.

Thirteen material properties are required (Table 2) to obtain the wave numbers $k(\omega)$. The ice density and bulk modulus are well known as well as the density, compressibility and viscosity of air. The remaining eight properties are specific to snow and must be determined for every sample. The snow density ρ_s can easily be measured to derive the porosity $\phi = 1 - \frac{\rho}{\rho_{ice}}$, whereas the other properties are more difficult to measure directly, but Sidler (2015) recently estimated most of the snow properties as a function of porosity. Johnson (1982) assumed that the dynamic coefficient ρ_{12} is zero. According to Sidler (2015), ρ_{12} can be approximated for a rigid solid phase by $\rho_{12} = -\phi\ \rho_{\mathrm{air}}(\Gamma - 1)$ (Carcione, 2007) and the tortuosity Γ can be calculated with $\Gamma = 1 - r(1 - \frac{1}{\phi}), r > 0$ (Berryman, 1980). We used the values for spherical grains $r = \frac{1}{2}$. The permeability κ, the pore characteristic size d, and the structure factor $\bar{d}$ are free parameters, which were varied within a physically reasonable range to fit the modeled attenuation to the measured values of the frequency dependent attenuation.

Using typical parameters for natural snow (Table 2) the speed of the fast and the transversal waves depends strongly on the elastic moduli of snow (E, ν), while the variation caused by the other parameters is below 1%. The speed can therefore be approximated as follows

$$c_{\mathrm{fast}} \approx \sqrt{\frac{E\,(1-\nu)}{\rho\,(1+\nu)(1-2\nu)}} \tag{3}$$

and

$$c_{\mathrm{transversal}} \approx \sqrt{\frac{E}{2\rho\,(1+\nu)}}, \tag{4}$$

which are the equations for the speed of longitudinal and transversal waves in an elastic medium with density ρ, Young's modulus E and the Poisson's ratio v. Therefore, the elastic moduli can be determined from the speed of the fast waves and the transversal waves. The speed and the attenuation of the slow waves are not influenced by the elastic moduli.

2.6. Simulation of propagation

The propagation of the PLF signal across the snow column was simulated assuming plane wave propagation with the complex wavenumbers $k(\omega)$ of the Biot's slow or fast waves. The propagation

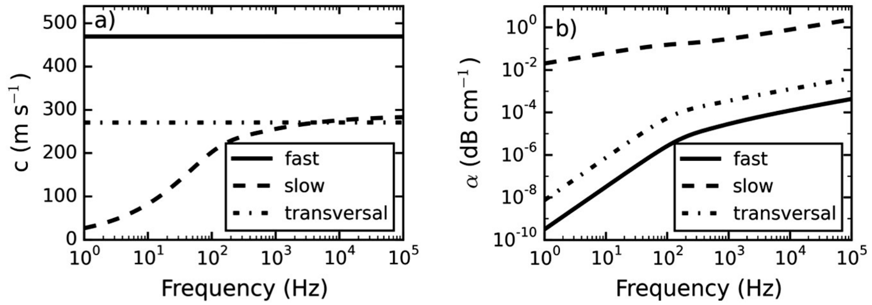

Fig. 4. (a) Dispersion relation of the three wave types of Biot's model and (b) attenuation coefficient α. These curves are obtained for typical values of the snow properties listed in Table 2.

Table 2
Parameters of Biot's model with typical values for snow. If available, the formula used to derive the parameter and a reference are listed. For air (*) the values depend on temperature and pressure; we used: $T = -25°$ to 0 °C, $p = 85$ kPa.

Material	Parameter	Symbol	Typical value	Formula	Source
Ice	Density	ρ_{ice}	$917\ \text{kg m}^{-3}$	–	(Hobbs, 1974)
	Bulk modulus	K	1.19×10^{9} Pa	–	(Johnson, 1982)
Air*	Density	ρ_{air}	$1.08-1.19\ \text{kg m}^{-3}$	–	(Bell et al., 2014)
	Compressibility	C_{air}	$(8.1-8.9) \times 10^{-6}\text{Pa}^{-1}$	–	(Bell et al., 2014)
	Kinematic viscosity	η	$(1.3-1.6) \times 10^{-5}\ \text{m}^2\ \text{s}^{-1}$	–	(Bell et al., 2014)
Snow	Density	ρ	50–500 kg m^3	Measured	–
	Porosity	ϕ	$0.45-0.95$	$\phi = 1-\frac{\rho}{\rho_{ice}}$	–
	Young's modulus	E	$0.2-10^{-4}$	$E = \rho c_t^2\ \frac{3c_f^2-4c_t^2}{(c_f^2-c_t^2)}$	(Mellor, 1975)
	Poisson's ratio	ν	$0.2-0.33$	$\nu = \frac{c_f^2-2c_t^2}{2(c_f^2-c_t^2)}$	(Mellor, 1975)
	Permeability	κ	$8.5\times 10^{-10}-10^{-8}\ \text{m}^2$	Fitting parameter	(Zermatten et al., 2011)
	Pore characteristic size	d	< 1 mm	Fitting parameter	estimated
	Structure factor	$\overline{d}$	1	Fitting parameter	chosen a priori
	Dynamic coefficient	ρ_{12}	$-(0.03-0.3)\text{kg m}^{-3}$	$\rho_{12} = \frac{1}{2}\phi\ \rho_{\text{air}}(1-\frac{1}{\phi})$	(Carcione, 2007)

was computed by Fourier transformation as described in Eq (5).

$$u(x_0,t) \xrightarrow{F.T.} \tilde{u}(x_0,\omega) \xrightarrow{Propagation} \tilde{u}(x_i,\omega)$$
$$= \tilde{u}(x_0,\omega)e^{i\ k(\omega)\ (x_i-x_0)} \xrightarrow{Inverse\ \ F.T.} u(x_i,t) \qquad (5)$$

First the discrete Fourier transformation of the source signal $u(x_0,t)$ was performed. Then the propagation was computed in the frequency domain multiplying each discrete frequency term with a transfer function ($e^{i\ k(\omega)\ (x_i-x_0)}$) dependent on the frequency dependent complex wave number $k(\omega)$ and the propagation distance (x_i-x_0). Eventually, an inverse Fourier transformation was performed to obtain the signal in time domain $u(x_i,t)$ at point x_i. A detailed description of the method is found in Doyle (1997). We used the signal measured by the sensor S2, i.e. the acoustic sensor at the bottom plate, at the shortest column length x_0 as source signal $u(x_0,t)$ to simulate the signal measured at the other column lengths x_i. The choice of signal of S2 as source allows comparing the simulated data to the measured data neglecting the effect of the snow-sensor coupling. The complex wavenumber $k(\omega)$ was determined fitting the Biot's model to the measured speed and attenuation. The amplitude and the energy of the propagated signal $u(x_i,t)$ at the different distances were determined as illustrated in Fig. 3a. The propagation speed of the simulated slow and fast wave pulses was computed from the time difference between the threshold crossing of the source signal and the threshold crossing of the propagated signal. The AIC method was not applied to the simulated signals because we wanted to investigate the effect of the attenuation on the speed determination.

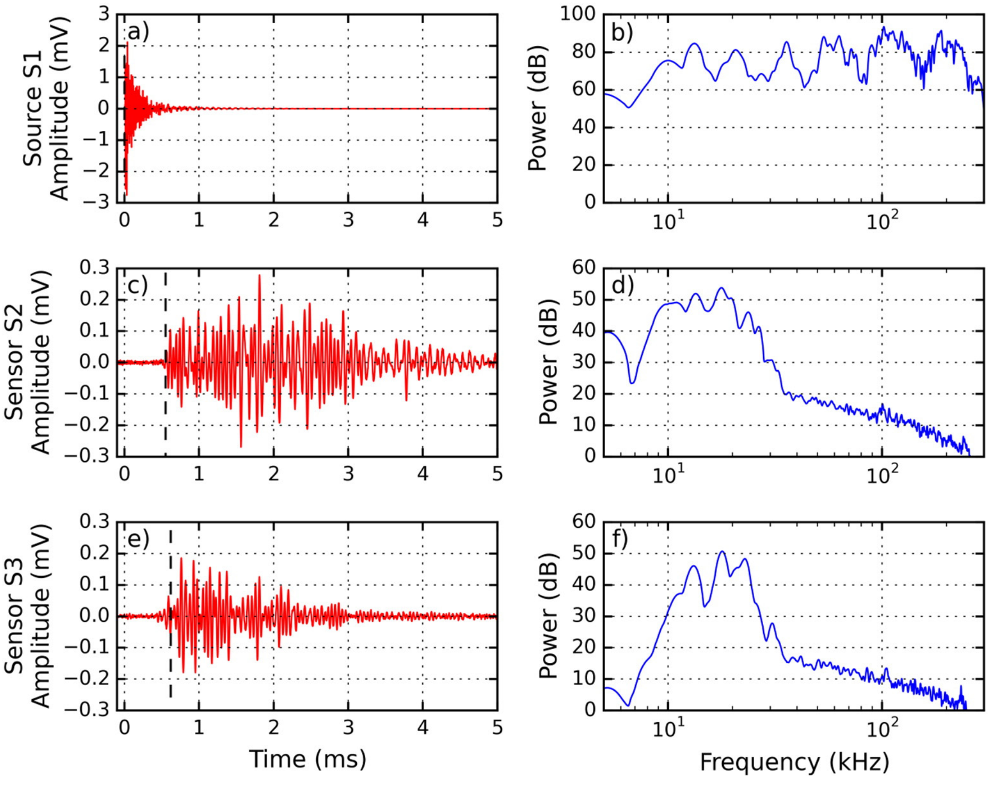

Fig. 5. (a,b) Exemplary results for the PLF signal and the corresponding power spectrum at the source, (b,c) recorded by sensor S2 after propagation through 19.5 cm of snow, and (e, f) recorded by sensor S3 placed at the side of the column at 18 cm from the top. All three signals were produced by the same PLF pulse on sample Col3A.

3. Results

3.1. PLF signals and power spectra

The PLF pulses propagating within snow were strongly distorted and attenuated. The evolution of a typical pulse before and after propagating through 19 cm of snow is illustrated in Fig. 5. The source PLF signal, measured before propagation in snow by the sensor S1, had a very sharp rising to the maximum amplitude and a fast decrease, while the amplitude of the signal recorded with the sensor S2 exhibited a more gradual increase and decrease (Fig. 5a, c). The duration of the signal was longer after propagation through snow. When measured by the sensor S2, the signal was 5 ms long, about five times longer than the source signal (Fig. 5b, d). The spectra of the signals after propagation differed strongly from the spectra before propagation. The power spectrum of the source signal was "flat", with almost constant frequency components from 8 kHz to 300 MHz, while the shape of the power spectrum after propagation was completely different. The frequencies above 40 kHz were very strongly attenuated. The main frequency components remaining were between 4 and 35 kHz, with the maximum of the power spectrum at 18 kHz. The signals measured with the sensor S3 were similar to the signals recorded by the sensor S2.

3.2. Propagation speed and Young's modulus

The acoustic speed measured by the sensor S2 at $h \approx 15$ cm is plotted as a function of snow density in Fig. 6a. All values are listed in Table 1. The speed measured at the sensor S2 was between 400 and 950 m s^{-1} and was higher for the samples with higher density. The propagation speed was measured for all column lengths h and was found to be constant up to a certain column length; for larger column lengths the speed decreased with increasing column length (Fig. 6b). The speed obtained with different PLF pulses was well reproducible. The mean deviation found for 10 to 20 pulses was between 1% and 7% for the values reported in Table 1. For longer columns lengths ($h > 30$ cm for Col1) for which the PLF signals are strongly attenuated the uncertainty increased. For these weaker and stronger distorted signals the onset was obscured by background noise and hence more difficult to determine, causing the higher uncertainty. The resulting speed is compared to the values reported in previous studies in Fig. 1.

For the sensor S3 it can be assumed that the first detected wave component followed the fastest path going first through the aluminum plate, where the speed is higher, and then through the snow (Fig. 7). Minimizing the travel time t with respect to the traveled distance in aluminum, the following equation for the sound speed in snow following the fastest path is found:

$$c_{\mathrm{snow}} = \frac{h_{S3}\, c_{\mathrm{al}}}{\sqrt{(t\, c_{\mathrm{al}} - r)^2 + h_{S3}^2}}, \tag{6}$$

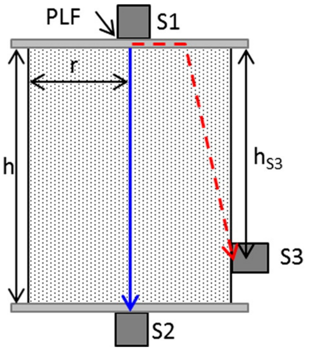

Fig. 7. Experimental setup with the wave paths used for the calculation of the wave speed. The red dashed line indicates the fastest path used for the sensor S3.

where c_{al} is the speed in the aluminum plate (3200 m s^{-1}), r is the column radius and h_{S3} is the vertical distance between the upper plate and the sensor S3. Using the fastest path, the speed measured by the sensor S3 was equal to the speed recorded by the sensor S2. It follows that the measured speed was that of longitudinal waves. The transversal wave component of the signal had a later arrival time and was superimposed on the rest of the signal and not recognizable. The employed method was therefore not suitable to measure the speed of transversal waves. The results described in the following were therefore all obtained from the signals measured by the sensor S2.

The Young's modulus E was calculated from the measured speed (Eqs. 3 and 4). Since the speed of the transversal waves could not be measured, it was not possible to derive the Poisson's ratio ν, which hence was chosen a priori $\nu = 0.25$ (Mellor, 1975; Shapiro et al., 1997). The resulting values of the Young's modulus E were between 30 and 340 MPa, and increased with increasing density (Table 1, Fig. 6a).

The results of the sintering experiments are presented in Figs.. 8 and 9. For both experiments the speed and the Young's modulus increased over time (Fig. 8). The increasing rate decreased with the sintering time. The speed measured in the first sintering experiment increased during the temperature increase as well as during the temperature decrease for both samples Col41 and Col42 (Fig. 8a).

The penetration force measured with the snow micro-penetrometer (SMP) increased also with increasing sintering time, with a fast increase during the first hours and a slower increase afterwards (Fig. 9a). The effective modulus derived from the SMP signal was clearly related to the Young's modulus calculated from the propagation speed, although the SMP-derived modulus was about 40 times smaller (Fig. 9b).

3.3. Attenuation

The attenuation coefficients α_{en} and α_{amp} of the entire pulse were derived from the pulse energy and the maximum amplitude (Fig. 10).

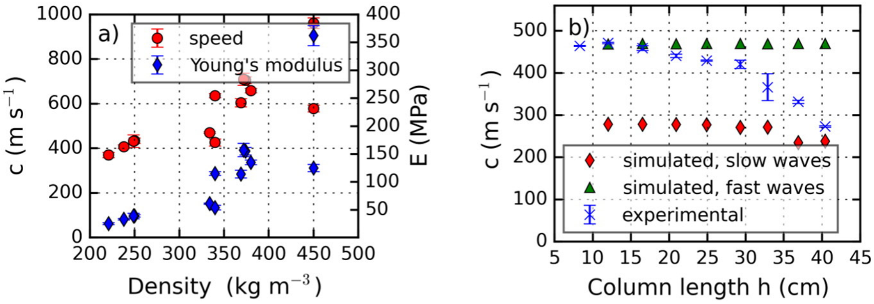

Fig. 6. (a) Speed c and derived Young's modulus E as a function of the density for the measured samples. The mean value and the standard deviation obtained from 10 to 20 PLF signals are shown (Table 1). (b) Speed measured on sample Col1 for different column lengths compared with the propagation speed of the simulated fast and slow wave pulses. For comparison to the modeled data the experimental data with threshold arrival time determination are shown.

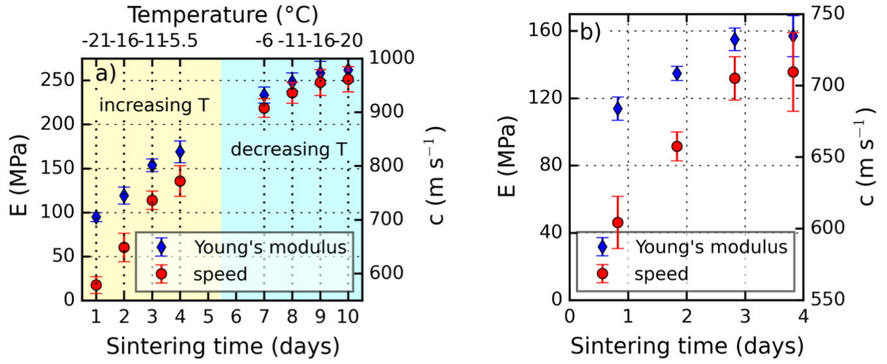

Fig. 8. (a) Increase of the wave speed *c* and the acoustically determined Young's modulus *E* with the sintering time for the sample Col41. The temperature *T* of the cold laboratory was increased stepwise during three days and subsequently decreased during another three days. The presented results are the average and the standard deviation (error bars) of 20 PLF signals at fixed column length $h = 15.7$ cm. (b) Increase of the wave speed *c* and the acoustic Young's modulus *E* with the sintering time for the sample Sam11 to Sam14. Every day a new sample was cut from the prepared snow block and the speed was measured for the successively shortened sample. The average and the standard deviation of the values obtained at 6 different column lengths between 12 cm and 18 cm are shown. The density is assumed to be constant over the entire duration of the experiments.

Both fits from either amplitude or energy provided similar results (Table 1). The resulting values were between 0.25 and 1.25 dB cm^{-1}. The attenuation coefficient seemed not to depend on density for our measurement setup and range of densities. Furthermore, in the second sintering experiment (Sam11 to Sam14), we did not observed any significant dependence of the attenuation coefficient on the sintering time. The precision of the measurements was, however, quite low. The coefficient of determination R^2 was between 0.85 and 0.15 (Table 1).

Fig. 11a shows the attenuation coefficient α as a function of frequency for sample Col1. The attenuation is only shown for the frequency band between 8 and 35 kHz for which the signal magnitude was sufficiently high to determine α with good precision. The attenuation coefficient α increased with increasing frequency for all samples for which it could be determined with good precision (Fig. 11b). It was between 0.3 and 1.6 dB cm^{-1}. The attenuation coefficient α of Biot's slow waves was fitted to the measured values using the permeability κ and the pore characteristic size *d* as fitting parameters (Fig. 11a). The value of the structure factor $\overline{d}$ was kept constant for simplicity. The obtained parameters for each sample are listed in Table 1. The obtained frequency dependent attenuation coefficient of the samples Sam11 to Sam14 had poor precision, because the attenuation was too low and the sample too short. Therefore, it is not shown.

The pulse energy and the maximum amplitude were extracted from the simulated signal and compared with the measured values at different propagation distances (Fig. 10). For the simulated slow wave pulses the amplitude and the energy decreased with increasing column height very similar to the decrease observed experimentally. On the other hand, for the simulated fast wave pulses the amplitude and the energy were almost constant for the various propagation distances.

In Fig. 6 the propagation speed of the simulated slow and fast wave pulses for the different column lengths is compared to the experimentally measured speed. The modeled speeds were almost constant for both the slow and fast wave pulses. The strong decrease in speed with increasing propagation distance observed in the experiments was not found for the simulated propagation of both wave types.

4. Discussion

The PLF signals after propagation through the snow column exhibited significant distortion and were nearly five times longer than the original length of the PLF signal. The distortion can be due, for example, to high frequency dependent attenuation, dispersive waves, superposition of wave types with different phase velocities, or waves following different paths. Usually, wave pulses with different arrival times can be separated using a longer propagation distance, but with our experimental setup this was not possible since the propagation distance is limited by the high attenuation. The sensor S3 attached at the lateral surface of the sample should have been more sensitive to the transversal waves, but the measured speed was that of longitudinal waves following the fastest path. Accordingly, we could not determine the speed of the transversal waves.

The speed measured by the sensor S2 at the bottom of the column corresponded to that of Biot's fast waves, since the speed of the first arriving wave packet was measured. The speed obtained with different PLF pulses was well reproducible with a mean deviation between 1% and 7% for a column length $h \approx 15$ cm. The difficulty to determine the exact arrival time is probably a main source of uncertainty. The measured speed was higher for higher densities, as can be expected for Biot's

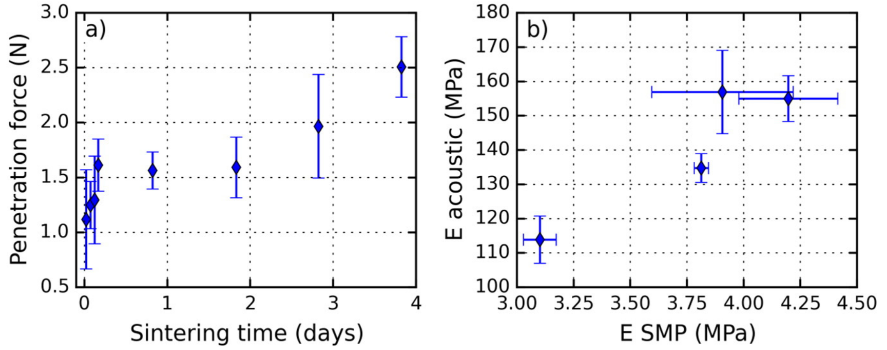

Fig. 9. (a) Effect of sintering time on the penetration force measured with the snow-micro-penetrometer (SMP) for the samples Sam11 to Sam14. (b) Comparison between the Young's modulus calculated from the propagation speed and the effective modulus derived from the SMP signal. The error bars of the SMP values are obtained from four repeated SMP measurements performed at different locations of the snow block for each time step.

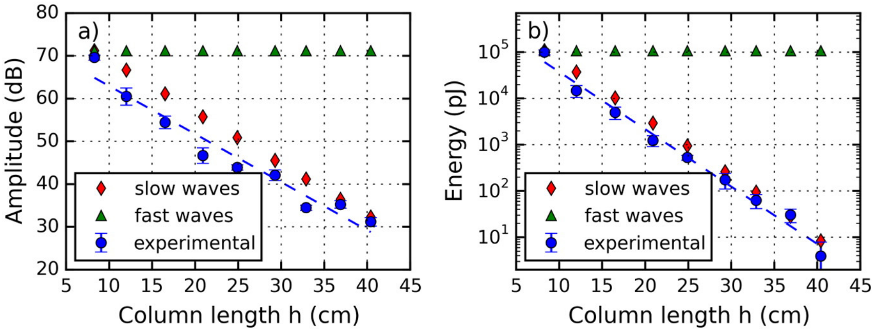

Fig. 10. (a) Maximum amplitude and (b) energy of the PLF pulse for different column lengths (sample Col1). The slope of the linear fit to the experimental data is equal to the attenuation coefficient ($\alpha_{en} = 1.2 \pm 0.1$ dB cm^{-1}, $\alpha_{amp} = 1.1 \pm 0.1$ dB cm^{-1}). The mean value and the standard deviation (error bars) of 20 PLF signals are shown. The experimental data are compared with the simulated data of Biot's slow and fast waves.

fast waves that propagate mainly through the ice skeleton. A similar behavior was found in the studies that measured the wave speed with sensors in direct contact with the snow (Fig. 1, Smith, 1965; Yamada et al., 1974; Takei and Maeno, 2004; Reiweger et al., 2015). Our speed values were lower than most literature values for similar densities (Fig. 1). The discrepancy may be due to different mechanical properties of the examined snow. Indeed, the sintering experiment clearly showed that snow of the same density can have different propagation speed and elastic properties. The values of the Young's modulus derived from the speed measurements were in good agreement with the data published by Mellor (1975); they were lower but correlated with the results obtained from micro-computed tomography images (Köchle and Schneebeli, 2014).

Both sintering experiments showed an increase in propagation speed, snow hardness, and Young's modulus with the time of sintering. This finding supports the interpretation that the speed measured was the speed of Biot's fast waves, since the speed of the slow waves is independent of the elastic properties of snow. The elastic moduli obtained with the acoustic method and derived from the SMP signal were related, but the SMP derived values were about 40 times lower than the acoustic values; the latter are more similar to the results obtained from micro-computed tomography images (Köchle and Schneebeli, 2014). The finding of the low values of the modulus derived from the SMP signal compared to other measurement methods has been previously reported (Kronholm, 2004; Reuter et al., 2013; Sigrist, 2006). The stresses applied to the snow microstructure during SMP measurements will likely cause non-elastic deformation, whereas the stress waves caused by the acoustic signal are in the elastic range. Nevertheless, the above mentioned studies have shown that the values of the SMP derived effective modulus were correlated with results of other measurement methods.

No direct influence of the temperature on the speed was measured (Col41 and Col42). The dependence of the speed on the temperature is assumed to be low, since it is known that the modulus of ice is just slightly temperature dependent (Sinha, 1989). The variation of the speed due to changes of the microstructure during the sintering time was therefore more relevant. The temperature influenced, however, the rate of change in the microstructure (Kaempfer and Schneebeli, 2007). Furthermore, the variation of the temperature and the resulting temperature gradients probably contributed to the changes in microstructure (Schneebeli and Sokratov, 2004).

The values of the attenuation coefficient (0.25–1.25 dB cm^{-1}) were in agreement with values published in previous studies (0.05–3.5 dB cm^{-1}) (Ishida, 1965; Lang, 1976; Johnson, 1982; Marco et al., 1998; Gudra and Najwer, 2011; Kapil et al., 2014; Reiweger et al., 2015). We recorded an increase in the attenuation with increasing frequency. The same behavior was observed for the modeled Biot's slow, transversal and fast waves. The magnitude of the measured attenuation coefficient was in the range of that of Biot's slow waves obtained with typical snow parameters, whereas the attenuation coefficient of the modeled Biot's fast and transversal waves was 3 to 4 orders of magnitude lower. Since the total energy of the pulses decreased by 4 orders of magnitude and the attenuation coefficient corresponds to that of the slow waves, we conclude that the majority of the energy traveled with Biot's slow waves. Johnson (1982) reported that for acoustic waves generated in air most of the energy is transmitted into snow through the air pores as Biot's slow waves and the slow waves are responsible for the strong attenuation. Our results showed that also in the case of waves generated in a metal plate in direct contact with the snow the majority of the energy travels through snow with the slow waves. This is in contrast to the literature values of speed which are different depending on the coupling (Fig. 1).

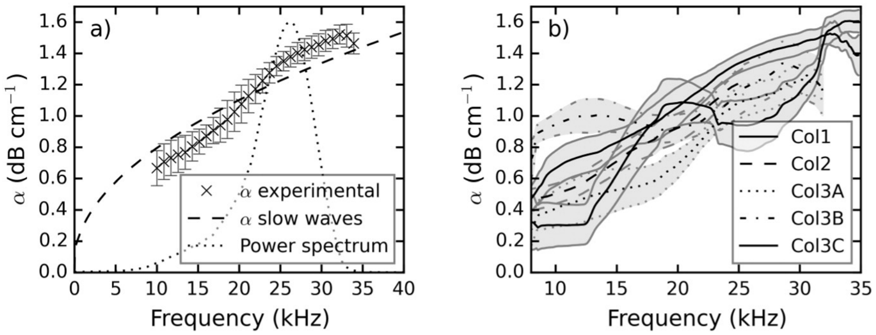

Fig. 11. (a) Attenuation coefficient α as a function of frequency determined from the measurements for sample Col1. The attenuation coefficient for Biot's slow wave is fitted to the experimental results varying the permeability κ and the pore characteristic size d. The power spectrum of a typical PLF signal after propagation in snow is shown (given in arbitrary units). The attenuation is reported for discrete frequency sets with intervals of 850 Hz. The error bars represent the standard error of the linear fit to the semi-logarithmical plot (See Fig. 3b). (b) Measured attenuation coefficient α as a function of frequency for the samples for which it could be determined.

A good fit of the modeled slow wave attenuation to the measured values in the frequency range of 10 to 35 kHz was obtained by varying the permeability and pore characteristic size, whereas the value of the structure factor $\overline{d}$ was kept constant for simplicity. In general, the application of Biot's model is limited by its complexity requiring a large number of parameters that are difficult to relate to the snow properties. With the parametrization proposed by Sidler (2015) the porosity is the only property required. We only used the porosity to express the dynamic coefficient ρ_{12}. In the future, the free fitting parameters permeability κ, pore characteristic size d, and structure factor $\overline{d}$ could directly be related to the snow microstructure. The permeability can be determined from the density and the grain size (Shimizu, 1970) or the specific surface area (SSA) (Calonne et al., 2012; Zermatten et al., 2011); the characteristic pore size can be calculated from 3-D microstructural data from micro-computed tomography (Hildebrand and Rüegsegger, 1997; Schneebeli and Sokratov, 2004).

The energy and maximum amplitude of the simulated pulses propagating with the slow waves agreed well with the measured values. This finding is not surprising, since the wave number used for the simulation of the propagation was obtained from the experimental values of the frequency dependent attenuation coefficient.

The propagation speed from the simulated fast and slow waves did not decrease with increasing column length as was observed in the measurements (Fig. 6). One could argue that a later arrival time and a lower speed should result if the signal amplitude decreases due to attenuation. Therefore, a decrease of the speed with increasing column length should be observed also for the modeled signals, since the arrival time of the modeled signals was determined by the crossing of a fixed threshold. As such a decrease was not observed for the modeled signals, we conclude that the lower speed measured with the longer columns is not due to an error in determining the arrival time caused by the signal attenuation.

We assumed plane waves and neglected geometric effects for the speed determination. This might as well be a reason of the lower speed with longer columns. In particular, the change in the ratio between length and width of the sample could have an influence on the measured speed. A propagation model, which takes into account the geometry of the sample, might provide better results.

The much stronger attenuation at frequencies higher than 35–40 kHz (Fig. 5) cannot be explained with Biot's model. This may be due to acoustic scattering effects at structural discontinuities of the ice skeleton that gain importance when the wavelength becomes comparable to the size of the snow structure. For waves with speed $c = 500$ m s^{-1} and frequency $\omega = 50$ kHz, the wavelength is $\lambda = \frac{c}{\omega} =$ 10 mm, which is comparable to the grain size of about 1 mm. The connection between sensor and snow could also be the source of the suppression of the frequencies above 35–40 kHz, but in previous AE experiments signals with peak frequencies in the 100–500 kHz range were measured with the same sensor type (Scapozza et al., 2004). These high frequency signals are presumably generated in the vicinity of the sensor, and the high frequency components are not attenuated due to the short propagation distance. Therefore, we conclude that high frequency suppression is not related to the snow-sensor coupling.

We could not find any significant change over time of the attenuation coefficient during the snow sintering experiment (Sam11 to Sam14, Table 1). Since the attenuation was rather low and the maximum column length was just 20 cm, the quality of the fits to the energy and maximum amplitude at the different column lengths was rather poor (R^2 between 0.15 and 0.85). Therefore, it is not possible to exclude a change of the attenuation coefficient over time. It is even quite probable, due to the changes of the snow microstructure over time.

5. Conclusions

Knowing the propagation characteristics of acoustic waves in snow is necessary for the identification and localization of AE features preceding snow failure. We measured the propagation speed and the attenuation of acoustic waves across different cylindrical snow samples.

The speed for the propagation of a PLF signal through a snow column was in the range of 300 to 950 m s^{-1} and corresponded to that of Biot's fast waves that mainly propagate through the ice skeleton of snow. From the speed, we derived the Young's modulus for different snow samples; it ranged from 33 MPa for a snow density of 240 kg m^{-3} to 340 MPa for a density of 450 kg m^{-3}. An increase of the SMP-derived effective elastic modulus with increasing time of sintering was observed. The frequency dependent attenuation was determined for the frequency range of 10 to 35 kHz and yielded values between 0.3 and 1.6 dB cm^{-1}, increasing with increasing frequency. The main frequencies of interest for snow failure studies (between 20 and 500 kHz, Datt et al., 2015; Reiweger et al., 2015; Scapozza et al., 2004) were found to have the highest attenuation coefficient. This is an important limitation for field applications where long propagation distances are not uncommon.

Comparing our experimental results with the propagation characteristics found by applying Biot's model suggests that the PLF signal propagated as a mixture of Biot's slow and fast waves. The majority of the energy was carried by the slow waves. On the other hand, Biot's model was not able to explain the strong attenuation observed for frequencies higher than 35 kHz, which is probably due to scattering at the ice skeleton. In general, the application of Biot's model is limited by its complexity requiring a large number of parameters that are difficult to relate to the snow properties.

Our findings on the propagation of sound in snow are helpful to characterize and localize acoustic emissions in snow, and hopefully to identify precursors to snow failure in view of assessing snow slope instability. Furthermore, we demonstrated that the employed method can be used for the non-destructive in-situ characterization of snowpack mechanical properties.

Acknowledgments

This project was funded by the Swiss National Science Foundation (SNF), project number 200021-146647. We thank Matthias Jaggi for support in the cold laboratory and Adrien Hildebrand for help with the experiments. We are further grateful to Alec van Herwijnen for helpful comments and suggestions. Comments provided by two anonymous reviewers helped to improve the paper.

Appendix

Deresiewicz and Rice (1962) found an analytical solution of Biot's equations for plane waves, which was applied to snow by Johnson (1982). The solution of the wave numbers $k(\omega)$ for the longitudinal fast and slow waves is:

$$k_{\text{fast,}\quad\text{slow}} = \sqrt{\frac{\rho^{*}\omega^{2}}{D+2N+2Q+R}\cdot\frac{B-i\,f\mp\sqrt{B^{2}-4AC-2i\,f(b-2A)-f^{2}}}{2A}} \tag{A1}$$

and

$$k_{\text{transversal}} = \sqrt{\frac{\rho^{*}\omega^{2}}{N}\cdot\frac{\frac{((1-\phi)\rho_{ice}-\rho_{12})(\phi\rho_{air}-\rho_{12}\cdot)-\rho_{12}^{2}}{\rho^{*2}}-i\,f}{\frac{\phi\rho_{air}-\rho_{12}\cdot}{\rho^{*}}-i\,f}} \tag{A2}$$

With:

$$A=\frac{(D+2N)R-Q^2}{(D+2N+2Q+R)^2},\qquad B=\frac{((1-\phi)\rho_{ice}-\rho_{12})R+(\phi\rho_{air}-\rho_{12})(D+2N)-2\rho_{12}Q}{\rho^*\,(D+2N+2Q+R)},$$

$$R=\frac{\phi^2}{\gamma+\frac{1}{K}-\frac{\tau}{K^2}},\qquad Q=\frac{\phi\left(1-\phi-\frac{\tau}{K^2}\right)}{\gamma+\frac{1}{K}-\frac{\tau}{K^2}},\qquad D=\frac{\gamma\tau+\phi^2+(1+2\phi)\left(1-\frac{\tau}{K}\right)}{\gamma+\frac{1}{K}-\frac{\tau}{K^2}},$$

$$N=\frac{E}{1+\nu},\qquad \gamma=\phi\left(C_{air}-\frac{1}{K}\right),\qquad \tau=\frac{E\,N}{9N-3E},\qquad \rho^*=(1-\phi)\rho_{ice}+\phi\rho_{air},$$

and the frequency dependent term: $f=\frac{\overline{d}\phi^2\frac{k^2T}{4k+8i\ T}}{\kappa\rho^*\omega}$,
with $k=d\sqrt{\frac{\omega}{\nu}}\,\overline{d}$ and $T=\frac{\mathrm{ber}'(k)+i\ \mathrm{ber}'(k)}{\mathrm{ber}(k)+i\ \mathrm{ber}(k)}$
where $\mathrm{ber}(k)$ and $\mathrm{ber}'(k)$ are the Bessel-Kelvin functions, and ω is the angular frequency.

References

Allard, J.F., Attala, N., 2009. Propagation of Sound in Porous Media: Modelling Sound Absorbing Materials. Wiley 372 pp.

Attenborough, K., Buser, O., 1988. On the application of rigid-porous models to impedance data for snow. J. Sound Vibr. 124 (2), 315–327.

Bell, I.H., Wronski, J., Quoilin, S., Lemort, V., 2014. Pure and pseudo-pure fluid thermophysical property evaluation and the open-source thermophysical property library CoolProp. Ind. Eng. Chem. Res. 53 (6), 2498–2508.

Berryman, J.G., 1980. Confirmation of Biot's theory. Appl. Phys. Lett. 37 (4), 382–384.

Biot, M.A., 1956a. Theory of propagation of elastic waves in a fluid-saturated porous solid. I. Low-frequency range. J. Acoust. Soc. Am. 28 (2), 168–178.

Biot, M.A., 1956b. Theory of propagation of elastic waves in a fluid-saturated porous solid. II. Higher frequency range. J. Acoust. Soc. Am. 28 (2), 179–191.

Boeckx, L., Jansens, G., Lauriks, W., Albert, D.G., 2004. Modelling acoustic surface waves above a snow layer. Acta Acust. united Ac. 90 (2), 246–250.

Buser, O., 1986. A rigid frame model of porous media for the acoustic impedance of snow. J. Sound Vibr. 111 (1), 71–92.

Calonne, N., Geindreau, C., Flin, F., Morin, S., Lesaffre, B., du Roscoat, S.R., Charrier, P., 2012. 3-D image-based numerical computations of snow permeability: links to specific surface area, density, and microstructural anisotropy. Cryosphere 6 (5), 939–951.

Carcione, J.M., 2007. Wave Fields in Real Media Wave Propagation in Anisotropic, Anelastic, Porous and Electromagnetic Media. Handbook of physical exploration. Seismic exploration, Elsevier, Amsterdam 515 pp.

Champoux, Y., Allard, J.F., 1991. Dynamic tortuosity and bulk modulus in air-saturated porous media. J. Appl. Phys. 70 (4), 1975–1979.

Datt, P., Kapil, J.C., Kumar, A., 2015. Acoustic emission characteristics and b-value estimate in relation to waveform analysis for damage response of snow. Cold Reg. Sci. Technol. 119, 170–182.

Deresiewicz, H., Rice, J.T., 1962. The effect of boundaries on wave propagation in a liquid-filled porous solid: III. Reflection of plane waves at a free plane boundary (general case). Bull. Seismol. Soc. Am. 52 (3), 595–625.

Doyle, J.F., 1997. Spectral Analysis of Wave Motion. In: Doyle, J.F. (Ed.), Wave Propagation in Structures. Mechanical Engineering Series, Springer New York, pp. 7–42.

Grosse, C.U., Ohtsu, M., 2006. Acoustic Emission Testing. Springer, Berlin, Germany 400 pp.

Gudra, T., Najwer, L., 2011. Ultrasonic investigation of snow and ice parameters. Acta Phys. Pol. A 120 (4), 625–629.

Higo, Y., Inaba, H., 1991. The General Problems of AE Sensors. In: Sachse, W., Roger, J., Yamaguchi, K. (Eds.), Acoustic Emission: Current Practice and Future Directions, ASTM STP 1077. American Society for Testing and Materials, Philadelphia, U.S.A., pp. 7–24.

Hildebrand, T., Rüegsegger, P., 1997. A new method for the model-independent assessment of thickness in three-dimensional images. J. Microsc. 185 (1), 67–75.

Hobbs, P.V., 1974. Ice Physics. Oxford University Press, London 837 pp.

Ishida, T., 1965. Acoustic properties of snow. Contrib. Inst. Low Temp. Sci. A20, 23–63.

Iwase, T., Sakuma, T., Yoshihisa, K., 2001. Measurements on sound propagation characteristics in snow layer. In: Alippi, A. (Ed.), 17th International Congress on Acoustics ICA, Rome, Italy, 2–7 September 2001, pp. 274–275.

Johnson, J.B., 1982. On the application of Biot's theory to acoustic wave propagation. Cold Reg. Sci. Technol. 6 (1), 49–60.

Johnson, J.B., Schneebeli, M., 1999. Characterizing the microstructural and micromechanical properties of snow. Cold Reg. Sci. Technol. 30 (1–3), 91–100.

Johnson, D.L., Koplik, J., Dashen, R., 1987. Theory of dynamic permeability and tortuosity in fluid-saturated porous media. J. Fluid Mech. 176, 379–402.

Kaempfer, T.U., Schneebeli, M., 2007. Observation of isothermal metamorphism of new snow and interpretation as a sintering process. J. Geophys. Res. 112 (D24), D24101.

Kapil, J.C., Datt, P., Kumar, A., Singh, K., Kumar, V., Satyawali, P.K., 2014. Multi-sensor couplers and waveguides for efficient detection of acoustic emission behavior of snow. Cold Reg. Sci. Technol. 101, 1–13.

Köchle, B., Schneebeli, M., 2014. Three-dimensional microstructure and numerical calculation of elastic properties of alpine snow with a focus on weak layers. J. Glaciol. 60 (222), 705–713.

Kronholm, K., 2004. Spatial Variability of Snow Mechanical Properties with Regard to Avalanche Formation Ph.D. Thesis University of Zurich, Zurich, Switzerland 192 pp.

Kurz, J.H., Grosse, C.U., Reinhardt, H.-W., 2005. Strategies for reliable automatic onset time picking of acoustic emissions and of ultrasound signals in concrete. Ultrasonics 43 (7), 538–546.

Lang, T.E., 1976. Measurements of acoustic properties of hard-pack snow. J. Glaciol. 17, 269–276.

Lee, S.M., Rogers, J.C., 1985. Characterization of snow by acoustic sounding: a feasibility study. J. Sound Vib. 99 (2), 247–266.

Marco, O., Buser, O., Villemain, P., Touvier, F., Revol, H.P., 1998. Acoustic impedance measurement of snow density. Ann. Glaciol. 26, 92–96.

Marshall, H.-P., Johnson, J.B., 2009. Accurate inversion of high-resolution snow penetrometer signals for microstructural and micromechanical properties. J. Geophys. Res. 114 (F4), F04016.

Maysenhölder, W., Heggli, M., Zhou, X., Zhang, T., Frei, E., Schneebeli, M., 2012. Microstructure and sound absorption of snow. Cold Reg. Sci. Technol. 83-84, 3–12.

McClung, D.M., Schaerer, P., 2006. The Avalanche Handbook. The Mountaineers Books, Seattle WA, U.S.A. 342 pp.

Mellor, M., 1975. A review of basic snow mechanics, Symposium at Grindelwald 1974 — Snow Mechanics. Int. Assoc. Hydrol. Sci. 114. IAHS Publ., Wallingford, U.K., pp. 251–291

Oura, H., 1953. Sound velocity in snow cover (in Japanese). Low Temp. Sci. Ser. A 9, 171–178.

Proksch, M., Löwe, H., Schneebeli, M., 2015. Density, specific surface area and correlation length of snow measured by high-resolution penetrometry. J. Geophys. Res. 120 (2), 346–362.

Reiweger, I., Schweizer, J., 2013. Measuring acoustic emissions in an avalanche starting zone to monitor snow stability. In: Naaim-Bouvet, F., Durand, Y., Lambert, R. (Eds.), Proceedings ISSW 2013International Snow Science Workshop, Grenoble, France, 7–11 October 2013. ANENA, IRSTEA, Météo-France, Grenoble, France, pp. 942–944.

Reiweger, I., Mayer, K., Steiner, K., Dual, J., Schweizer, J., 2015. Measuring and localizing acoustic emission events in snow prior to fracture. Cold Reg. Sci. Technol. 110, 160–169.

Reuter, B., Proksch, M., Löwe, H., van Herwijnen, A., Schweizer, J., 2013. On how to measure snow mechanical properties relevant to slab avalanche release. In: Naaim-Bouvet, F., Durand, Y., Lambert, R. (Eds.), Proceedings ISSW 2013International Snow Science Workshop, Grenoble, France, 7–11 October 2013. ANENA, IRSTEA, Météo-France, Grenoble, France, pp. 7–11.

Scapozza, C., Bucher, F., Amann, P., Ammann, W.J., Bartelt, P., 2004. The temperature-and density-dependent acoustic emission response of snow in monoaxial compression tests. Ann. Glaciol. 38, 291–298.

Schleef, S., Jaggi, M., Löwe, H., Schneebeli, M., 2014. An improved machine to produce nature-identical snow in the laboratory. J. Glaciol. 60 (219), 94–102.

Schneebeli, M., 2004. Numerical simulation of elastic stress in the microstructure of snow. Ann. Glaciol. 38, 339–342.

Schneebeli, M., Johnson, J.B., 1998. A constant-speed penetrometer for high-resolution snow stratigraphy. Ann. Glaciol. 26, 107–111.

Schneebeli, M., Sokratov, S.A., 2004. Tomography of temperature gradient metamorphism of snow and associated changes in heat conductivity. Hydrol. Process. 18 (18), 3655–3665.

Schweizer, J., 2008. On the predictability of snow avalanches. In: Campbell, C., Conger, S., Haegeli, P. (Eds.), Proceedings ISSW 2008, International Snow Science Workshop, Whistler, Canada, 21–27 September 2008, pp. 688–692.

Shapiro, L.H., Johnson, J.B., Sturm, M., Blaisdell, G.L., 1997. Snow mechanics — Review of the state of knowledge and applications. CRREL Report 97–3, US Army Cold Regions Research and Engineering Laboratory, Hanover, N.H., U.S.A.

Shimizu, H., 1970. Air permeability of depositied snow. Contrib. Inst. Low Temp. Sci. A22, 1–32.

Sidler, R., 2015. A porosity-based Biot model for acoustic waves in snow. J. Glaciol. 61 (228), 789–798.

Sidler, R., Simioni, S., Dual, J., Schweizer, J., 2016. Numerical simulation of wave propagation and snow failure from explosive loading. Cold Reg. Sci. Technol. submitted.

Sigrist, C., 2006. Measurement of Fracture Mechanical Properties of Snow and Application to Dry Snow Slab Avalanche Release Ph.D. Thesis ETH Zurich, Zurich, Switzerland 139 pp.

Simioni, S., Sidler, R., Dual, J., Schweizer, J., 2015. Field measurements and modeling of wave propagation and subsequent weak layer failure in snow due to explosive loading. Geophys. Res. Abstr. 17, EGU2015–EGU8706.

Sinha, N.K., 1989. Elasticity of natural types of polycrystalline ice. Cold Reg. Sci. Technol. 17 (2), 127–135.

Smith, J.L., 1965. The elastic constants, strength and density of Greenland snow as determined from measurements of sonic wave velocity. CRREL Technical Report 167. U.S.A, US Army Cold Regions Research and Engineering Laboratory, Hanover NH.

Sommerfeld, R., 1982. A review of snow acoustics. Rev. Geophys. Space Phys. 20, 62–66.

Sommerfeld, R.A., Gubler, H., 1983. Snow avalanches and acoustic emissions. Ann. Glaciol. 4, 271–276.

Takei, I., Maeno, N., 2004. Mechanical vibration responses of snow samples near the melting temperature. Ann. Glaciol. 38 (1), 130–134.

Wilson, D.K., 1993. Relaxation-matched modeling of propagation through porous media, including fractal pore structure. J. Acoust. Soc. Am. 94 (2), 1136–1145.

Wilson, D.K., 1997. Simple, relaxational models for the acoustical properties of porous media. Appl. Acoust. 50 (3), 171–188.

Yamada, T., Hasemi, T., Izumi, K., Sata, A., 1974. On the dependencies of the velocities of P and S waves and thermal conductivity of snow upon the texture of snow. Contrib. Inst. Low Temp. Sci. A32, 71–80.

Zermatten, E., Haussener, S., Schneebeli, M., Steinfeld, A., 2011. Tomography-based determination of permeability and Dupuit–Forchheimer coefficient of characteristic snow samples. J. Glaciol. 57 (205), 811–816.

Zwikker, C., Kosten, C.W., 1949. Sound Absorbing Materials. Elsevier 174 pp.